Geophysical Prospecting

EAGE EUROPEAN ASSOCIATION OF GEOSCIENTISTS & ENGINEERS

Geophysical Prospecting doi: 10.1111/j.1365-2478.2012.01120.x

Influence of a velocity model and source frequency on microseismic waveforms: some implications for microseismic locations

P.J. Usher,[1,3] D.A. Angus[2,3]* and J.P. Verdon[1]

[1]*Department of Earth Sciences, University of Bristol, Bristol, UK,* [2]*CiPEG, University of Leeds, Leeds, UK, and* [3]*School of Earth & Environment, University of Leeds, Leeds, UK*

Received July 2011, revision accepted June 2012

ABSTRACT

In this paper, we examine the influence of a velocity model and microseismic source frequency on microseismic waveforms and event locations. Finite-difference waveform synthetics are generated based on the Cotton Valley hydraulic fracture experiment, where we vary the vertical heterogeneity of the velocity models as well as the microseismic source frequencies. We find that differences between plausible velocity models lead to changes in arrival times of approximately 0.0035 seconds for P-waves and 0.0085 seconds for S-waves. Based on the average P- and S-wave velocities, the difference in the P- and S-wave traveltimes is equivalent to approximately 20 m in location difference. Significant increases in the waveform coda develop with increasing model heterogeneity and increasing source frequency. The presence of signal noise as well as other sources of error (e.g., uncertainty in geophone location) will likely lead to further increase in uncertainty in location error estimates. Thus we note that location error due to incorrect velocity models cannot be ignored.

Keywords: Microseismicity, Source frequency, Velocity model, Waveforms.

1 INTRODUCTION

Microseismicity is ideally suited and actively used to study the state of stress and fracturing in rock mass (e.g., Gibowicz and Kijko 1994). Monitoring the distribution of microseismic attributes (e.g., event location and source mechanism) in space and in time provides insight into the spatial and temporal variations in the stress field and is commonly used to delineate activity on pre-existing faults and joint systems as well as identify their orientation and density. Hence, over the past couple of decades, microseismic monitoring has become increasingly common in the hydrocarbon industry as a tool to investigate production related geomechanical deformation (such as subsidence, e.g., Dyer *et al.* 1999) as well as audit hydraulic fracture stimulation treatments (e.g., Maxwell and Urbancic 2005). Waveform attributes, such as amplitude and polarity, can be used to invert for the failure mechanisms (e.g., moment tensors) of both pre-existing and newly generated fractures or fracture systems (e.g., Baig and Urbancic 2010), as well as evaluate the fracture stimulation program (e.g., Baig *et al.* 2011). As a passive source, microseismicity can be used to characterize spatial and temporal variations in seismic attributes (e.g., seismic anisotropy) within the rock mass between the source and receiver (e.g., see Verdon and Kendall 2011, for estimating fracture orientation and density).

The application of microseismic monitoring to characterize fracturing and fracture systems within reservoirs is playing a greater role in reservoir management due to improvements in instrumentation, processing and interpretation. This is certainly true for unconventional reservoirs (e.g., tight-gas sands and shale gas), where there is a greater stress sensitivity of fluid flow compared to conventional reservoirs (e.g., Al Rajhi *et al.* 2010) and for the geological storage of CO_2, where monitoring top-seal and well-bore integrity is paramount in assessing risk and long-term confinement (e.g., Verdon *et al.* 2011). A

*E-mail: D.Angus@Leeds.ac.uk

general effect of velocity model error is the offset of seismic events from their true location (e.g., injection point). Thus, the ability to accurately locate microseismic events is becoming increasingly important for advanced microseismic techniques that characterize fractures in detail and hence for informed reservoir management. Although the location of microseismic events is the most fundamental measurement in microseismic monitoring, location error analysis generally involves estimating traveltime residuals with very little importance attributed to the influence of the velocity model (Maxwell 2010; Maxwell *et al.* 2010b). Foulger and Julian (2012) provided a recent and thorough discussion on the importance of location accuracy and the necessity of reliably quantifying location error.

Location errors stem from limitations due to monitoring array geometry (e.g., Eisner *et al.* 2009; Jansky, Plicka and Eisner 2010) as well as uncertainty in traveltime picks (e.g., Eisner *et al.* 2010), event azimuths (e.g., Jones *et al.* 2010) and velocity model. Probably least well understood is the impact of the velocity model error on location accuracy. In this paper, we study the influence of the velocity model and source frequency on microseismic waveforms and explore how these parameters might influence location. To do this, we generate synthetic waveform data using the finite-difference method to assess the impact of the frequency dependence of seismic waveforms due to velocity model heterogeneity. Although the influence of velocity model heterogeneity on band-limited waveforms seems intuitive (e.g., Angus 2005), finite-frequency effects are often overlooked in location error studies. For instance, although ray-based approaches (i.e., high-frequency asymptotic solutions) provide valuable contributions to our understanding of velocity models and locations (e.g., Eisner *et al.* 2009), they do not consider the influence of velocity variations on the order of or less than the seismic wavelength. To facilitate comparison with observed microseismic waveforms and hence help provide qualitative justification for our synthetic study, the synthetic model used in this study is based on the Cotton Valley hydraulic fracture experiment (see Walker 1997; Rutledge, Phillips and Mayerhofer 2004).

2 MICROSEISMIC LOCATION

The location of a microseismic event tells us where and when the rock mass is undergoing elastic failure. For instance, if we consider the case of hydraulic fracture stimulation, the microseismic event location provides a means to monitor and potentially manage the geometry of stimulated fractures. If the fracturing progresses outside the perforation or injection interval (e.g., reservoir bed), this can have important economical and environmental consequences, either in terms of loss of hydrocarbon or leakage of CO_2. As well, monitoring the number of events within each bed can be used to quantify the seismic injection efficiency of each bed (Maxwell *et al.* 2008). Thus, improving location accuracy will lead to higher resolution imaging of features. Furthermore, any error associated with event location will be passed on to any subsequent interpretation and/or estimates of other microseismic attributes, such as source mechanism (e.g., Angus 1998) or seismic anisotropy (e.g., Verdon and Kendall 2011).

There are three main techniques for locating microseismic events (Maxwell *et al.* 2010a): triangulation, hodogram and semblance based techniques. The triangulation technique uses P-wave and/or S-wave arrival time picks from numerous stations to locate microseismicity. The event time and spatial location can be estimated using arrival time phase picks and a velocity model. The hodogram technique uses the particle motion of the P-wave phase, where the particle motion is polarized along the direction of wave propagation. From the particle motion, the azimuth to the earthquake can be found. For single-station or single-borehole arrays, there is a 180° ambiguity in azimuth and incorporation of a dip is often needed (e.g., Jones *et al.* 2010). For the hodogram approach, traveltime phase picks and a velocity model are required. The semblance technique (e.g., Duncan and Eisner 2010) is similar to migration and involves propagating the microseismic energy back to its hypocentre using a Green's function (e.g., Kirchhoff, Gaussian beam and one-way wave equation migration) and does not require arrival time phase picks (e.g., Rentsch *et al.* 2007; Duncan and Eisner 2010). It is important to stress that in all three approaches a velocity model is required. Yet the velocity model may be poorly constrained and is often neglected within location error analysis.

Over the past several decades there have been a variety of studies that have explored the quantification of location error. For instance, Pavlis (1986) looked at the combination of different sources of error on location accuracy, including source-receiver geometry, velocity model and phase picking. In general, error analysis considers only the misfit between the observed and predicted data using what is assumed to be a well-known velocity model (e.g., Zimmer *et al.* 2007). It is generally, yet incorrectly, interpreted that as the estimation of location error approaches zero, the estimated event location approaches that of the true event location. More recently, however, the influence of the velocity model on location has been given greater consideration (e.g., Eisner *et al.* 2009; Maxwell 2009). For instance, Urbancic, Morrish and

Shumila (2009) provided a statistical estimate of event location using confidence limits and is similar to the approach developed by Foulger and Julian (2012) for geothermal applications. Yet few of these studies consider the influence of the velocity model on band-limited seismic waveforms, where even weak heterogeneity can significantly influence seismic waveforms and wavefronts (e.g., Angus 2005).

3 VELOCITY MODEL

There are many different types of velocity models available for a reservoir. Active-source surface seismic surveys provide large volume maps of a reservoir but have relatively low vertical and horizontal resolution. On the scale of hydraulic stimulation, the sub-volume of stimulated rock mass may appear relatively homogeneous within surface seismic velocity models. Vertical seismic profile (VSP) surveys generally provide higher spatial resolution (predominantly vertical) than active surface but at a loss of horizontal spatial sampling (i.e., the velocity model becomes more localized around the borehole). Sonic velocity logs provide the highest resolution in terms of vertical structure but very little if any lateral information. The choice of velocity model in microseismic event location depends on availability, how well it performs in locating calibration shots and the array geometry. Often, a velocity model might be modified to ensure that perforation shots, which have a known location, are located accurately.

Possible microseismic monitoring arrays include borehole arrays, surface arrays, or a combination of borehole and surface arrays. Downhole arrays are generally located close to the anticipated microseismicity and so the recorded microseismic waveforms will have relatively high-frequency content compared to surface microseismicity, due to minimal attenuation and geometrical spreading. Sonic velocity logs and VSP velocity models may be more suitable for such scenarios. Surface microseismic arrays are normally set out along grids on the surface, or placed in shallow boreholes (typically 50–200 m) to reduce surface noise and higher attenuation in near-surface layers. As surface arrays are located further away from the event hypocentres in comparison to borehole arrays, microseismic waveforms recorded at the surface suffer from a low signal-to-noise ratio due to geometrical spreading and attenuation. Thus surface microseismic monitoring often requires waveform stacking (e.g., Duncan and Eisner 2010) and migration based location techniques (e.g., Chambers *et al.* 2010). Surface seismic and/or VSP type velocity models may therefore be more suitable for surface seismic location processing.

Given the range of velocity models with differing spatial resolution, an informed choice in the velocity model used in locating microseismicity is required and a better understanding of the influence of the velocity model on location error is advisable. For hydraulic stimulation, sonic velocity models are commonly used to locate microseismic events (see Maxwell *et al.* 1998 and others). Sonic velocity models are ideal primarily due to their availability as well as the fact that the sonic frequencies (e.g., up to 2 kHz, Bulant and Klimeš 2008) are within the upper range of typical microseismic events (e.g., 10's to 100's of Hz). However, lithology plays an important role, where it has been observed that in certain settings the velocity contrasts are relatively weak such that a smooth model is sufficient and in other settings the velocity contrasts are severe enough that headwaves are pervasive and problematic such that a smooth model is likely insufficient (Zimmer 2011, pers. comm.).

In this study, we synthesize three velocity models to mimic the types of velocity model that can be generated from a surface seismic survey, a VSP survey and a sonic log using data from the Cotton Valley, East Texas Basin, U.S., hydraulic fracture experiment (see Walker 1997). The main reason for choosing Cotton Valley is because it has been extensively studied (see Rutledge *et al.* 2004 and references therein) and allows for direct comparison with observed microseismic waveforms. Cotton Valley is a tight-gas reservoir and hence has low permeability. Therefore it has undergone two stages of hydraulic stimulation: an injection stage using a gel treatment and an injection stage using a water treatment. The microseismic activity is located approximately at a depth of 2.5 km and so we limit our synthetic velocity models (and simulations) to within the depth range of 2–3 km. We use the sonic velocity log data from the well located closest to the injection point (well CGU 21-10) to derive our synthetic VSP and sonic velocity models. This log contains both P- and S-wave sonic velocity data.

Figure 1 displays the sonic log and the three synthetic velocity models derived for our synthetic study. Based on numerical consideration (microseismic source frequency and finite-difference dispersion criteria discussed in the following section), the sonic velocity log for well CGU 21-10 was decimated to a 34 layer model (layer thickness of approximately 30 m). O'Brien and Harris (2006) provided a VSP model for Cotton Valley but only to a depth shallower than the region of interest. Thus, the constructed VSP model for this study was aided by the observed characteristics provided by O'Brien and Harris (2006). The VSP model is defined by 13 discrete layers consistent with the derived sonic log (layer thickness on the

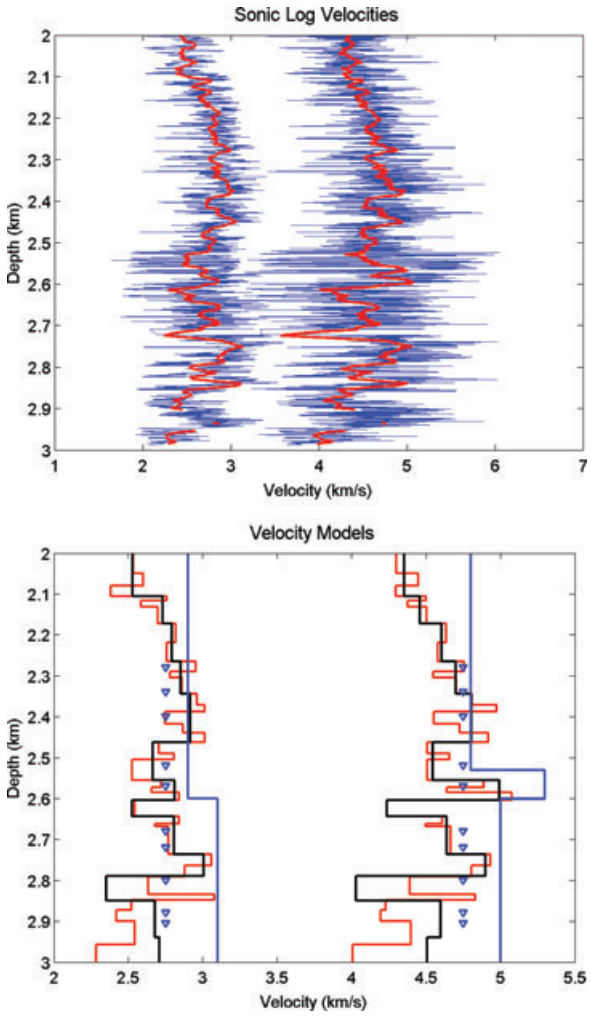

Figure 1 Top: sonic velocity log (blue) and filtered version (red) for well CGU 21-10. Bottom: synthetic P- and S-wave velocity models for the Cotton Valley hydraulic experiment; surface seismic model (blue), VSP model (black) and sonic model (red).

order of 75 m). The surface seismic velocity model is based on the three-layer model used by Rutledge and Phillips (2003).

4 MICROSEISMIC WAVEFORM MODELLING

Ray-based methods are commonly used to quantify the influence of a velocity model on microseismic event locations and their error (e.g., Eisner *et al.* 2009; Maxwell 2009; Jansky *et al.* 2010). However, ray-based approaches neglect frequency-dependent effects and non-geometrical arrivals (e.g., head waves) and are generally only suitable for smooth velocity models (i.e., when heterogeneity length scales are greater than the dominant seismic wavelength). The range of microseismic source frequencies observed in microseismic monitoring can vary widely and depends on the strength of the stress redistribution (e.g., injection pressure) as well as the length scales of the internal material weaknesses (e.g., pre-existing fractures and joints) present within the rock mass (Gibowicz and Kijko 1994). In theory, low-magnitude microseismic events typically have a higher dominant frequency than larger magnitude events and this relates to the size of the rupture surface initiated by failure. In practice, however, the range of recorded source frequencies will be more restricted and depends on the scale of the monitoring program (i.e., the size and distribution of the acquisition geometry), the sensitivity and coupling of the instrumentation, the presence of background noise (e.g., operational noise) and path effects (e.g., attenuation).

Assuming P- and S-wave velocities 4750 m/s and 3000 m/s, respectively, a 40 Hz microseismic event will have a dominant wavelength on the order of 100 m whereas a 150 Hz microseismic event will have wavelength of 30 m. If the true velocity model has velocity heterogeneity on the order of 100 m or less, frequency-dependent waveform effects will be significant (Angus 2005). For such a scenario, ray theoretical approaches may be neglecting important wave phenomena and hence full waveforms synthetics may be needed to capture frequency-dependent effects. However, full waveform synthetic studies have rarely been performed, most likely because full waveform algorithms, such as the finite-difference method, can be computationally expensive.

In this study, we use the full waveform E3D code (Larsen and Harris 1993) to generate synthetic waveforms. E3D is a staggered grid, fourth-order accurate in space and second-order accurate in the time finite-difference algorithm for isotropic two-dimensional (2D) and three-dimensional (3D) viscoelastic media. It has been used recently to model microseismicity in hard-rock mining applications to benchmark an automated event location algorithm (Gharti *et al.* 2010) and this study was the impetus for using E3D to examine microseismic waveform effects. The synthetic microseismic sources and reservoir model were designed to mimic the Cotton Valley hydraulic fracture experiment (Walker 1997) to enable us to qualitatively relate the numerical simulations to real observed microseismic data.

4.1 Microseismic source

There are over 800 recorded events in the Cotton Valley data set and so we selected a synthetic source location within the middle of the recorded seismicity (see asterisk between wells

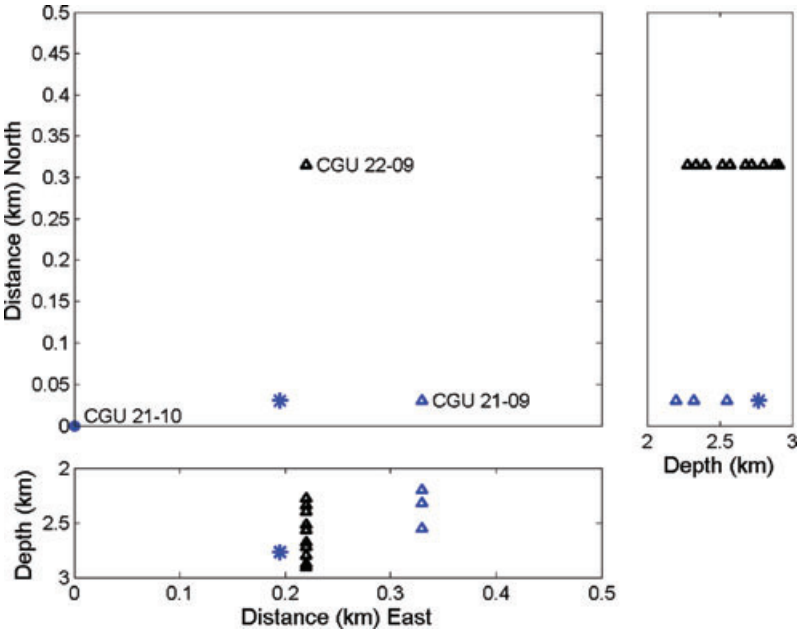

Figure 2 Location of the boreholes in map view (top) and the location of the geophones (triangles) in the cross-section (right and bottom). The location of the modelled source is indicated by the star. The two monitoring boreholes CGU 22-09 and CGU 21-09 are labelled as well as the injector well CGU 21-10.

CGU 21-10 and CGU 21-09 in Fig. 2). The location of the microseismic event is kept constant in all simulations to focus solely on the influence of velocity model dependence as well as source frequency dependence in the synthetic waveforms. To be consistent with events recorded at Cotton Valley, the source parameters are derived from the inverted focal solutions of Rutledge *et al.* (2004), where the dominant source mechanism is a strike-slip with approximate north-south, east-west striking nodal planes and a dip of approximately 85°.

As discussed earlier, the range of source frequencies can vary depending on several factors. In a previous study of Cotton Valley microseismicity, Rentsch *et al.* (2007) observed a dominant frequency of 100 Hz. It is not uncommon, however, to observe dominant frequencies down to the 10's of Hz (e.g., Teanby *et al.* 2004) and up to the 100's Hz (e.g., Trifu, Angus and Shumila 2000). Therefore, to capture a realistic range of source frequencies, we simulate three source frequencies at 40 Hz, 150 Hz and 300 Hz. Based on Urbancic and Zinno (1998), we define the microseismic moment magnitude to be 4.4×10^{10} dyne.cm for all source frequencies. We keep the size of the seismic moment constant in all simulations to facilitate waveform comparisons but note here that the source moment magnitude would be smaller for higher dominant frequency sources and larger for lower dominant frequency sources (e.g., see Izutani and Kanamori 2001, Fig. 4). For most microseismic analysis (with the exception of rockburst studies in mining), the elastic medium is linear elastic and hence differences in source moment magnitude translates into differences in waveform amplitude and not shape (e.g., Liner 2004).

4.2 Model geometry

The locations of the model geophone arrays and the synthetic microseismic source are shown in Fig. 2. This is based on the field configuration shown in Fig. 1 of Rutledge *et al.* (2004). For the simulations, we assume that the geophone arrays are vertical (i.e., no lateral borehole deviation). For the gel treatment (i.e., the second stage of injection), the injector well is CGU 21-10 and the monitoring arrays are CGU 22-09 and CGU 21-09 (with average vertical geophone spacing of 70 m). Array CGU 22-09 consists in 10 working geophones, whereas CGU 21-09 consists in 3 working geophones. For the water treatment (i.e., the first stage of injection), the injection well is CGU 21-09 and only the single borehole array CGU 22-09 is used to record microseismicity. To model the microseismic waveforms of the gel treatment, the multiple arrays were modelled as two separate 2D vertical profiles (e.g., vertical plane through the source and respective borehole array).

Reducing the problem from 3D to 2D can be justified because the velocity models are only depth dependent and in doing so allows for a significant reduction in computational resources. It should be noted that modelling the 3D problem using a 2D simplification decreases the accuracy of the computed synthetics (e.g., Liner 2004). However, since we are concerned mainly with traveltime anomalies and relative waveform (e.g., amplitude) perturbations, the reduction to 2D is sufficiently accurate for our purposes. However, this simplification can be problematic if absolute amplitude variations are required. This is because 2D modelling does not calculate the amplitude correctly due to geometric spreading (i.e., in 3D the amplitude decay is proportional to $1/r$ and in 2D is proportional to $1/\sqrt{r}$). Thus, if significant lateral heterogeneity is expected or if absolute amplitudes are required (e.g., for moment tensor analysis), full 3D simulation would be necessary.

In all simulations, the model has a lateral extent of 5000 m and a vertical extent of 1000 m. The density of the model is constant throughout at 3000 kg/m^3. Since we are modelling a sub-volume at depth, all four boundaries are set as absorbing boundaries (Clayton and Engquist 1977). To minimize numerical dispersion, satisfy numerical stability and maintain computational efficiency, the grid and time parameters for all source frequencies vary. Specifically, we define the grid increment Δh such that we have at least 10 grid points per minimum wavelength λ_{min}, $\Delta h = \lambda_{min}/10$ (e.g., Alford, Kelly and Boore 1974) and define the time increment Δt such that the relationship $\Delta t \leq 0.606\Delta h/V_{max}$ holds, (e.g., Kelly *et al.* 1976), where V_{max} is the maximum velocity. For the 40 Hz source, the grid spacing is 6 m with a time increment of 0.6 ms and total time samples of 600. For the 150 Hz source, the grid spacing is reduced to 1 m with a time increment of 0.1 ms and total time samples of 3600. For the 300 Hz source, the grid spacing required is 0.5 m with a time increment of 0.056 ms and 6100 time samples.

5 SYNTHETIC WAVEFORM RESULTS

To increase our understanding of the influence of the velocity model on microseismic waveforms and implications for microseismic locations, we generate synthetic waveforms while varying the velocity model, the microseismic source frequency and the array geometry (specifically geophone proximity). For most of the simulations, we model the single array CGU 22-09 because it consists in 10 geophones and allows for greater waveform comparison. Since all simulations are 2D, the synthetic traces have horizontal (x) and vertical (z) components. All trace amplitudes are normalized to the largest amplitude within the geophone array.

5.1 Sensitivity to velocity model

To compare the influence of velocity models, we simulate three microseismic events with a double-couple source having strike 80° and dip 85° and source frequencies of 40 Hz, 150 Hz and 300 Hz, respectively. The results for each velocity model are shown in Fig. 3 for the 40 Hz case, in Fig. 4 for the 150 Hz

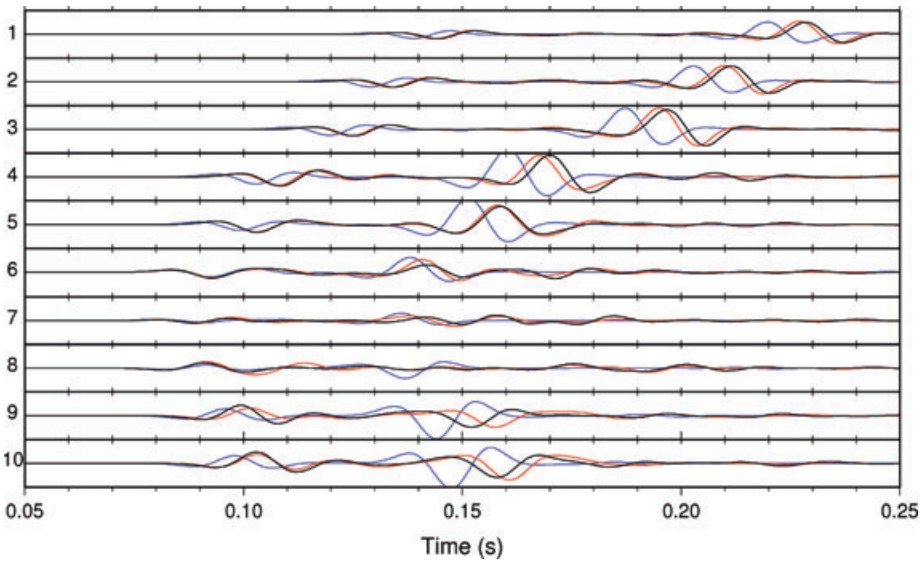

Figure 3 Comparison of 40 Hz waveforms for the surface seismic (blue), VSP (black) and sonic (red) velocity models.

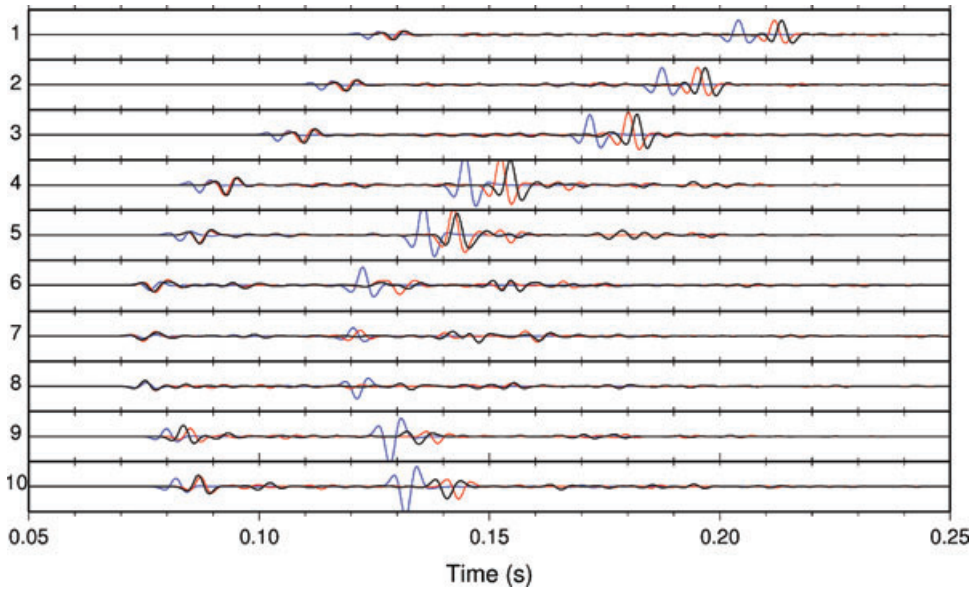

Figure 4 Comparison of 150 Hz waveforms for the surface seismic (blue), VSP (black) and sonic (red) velocity models.

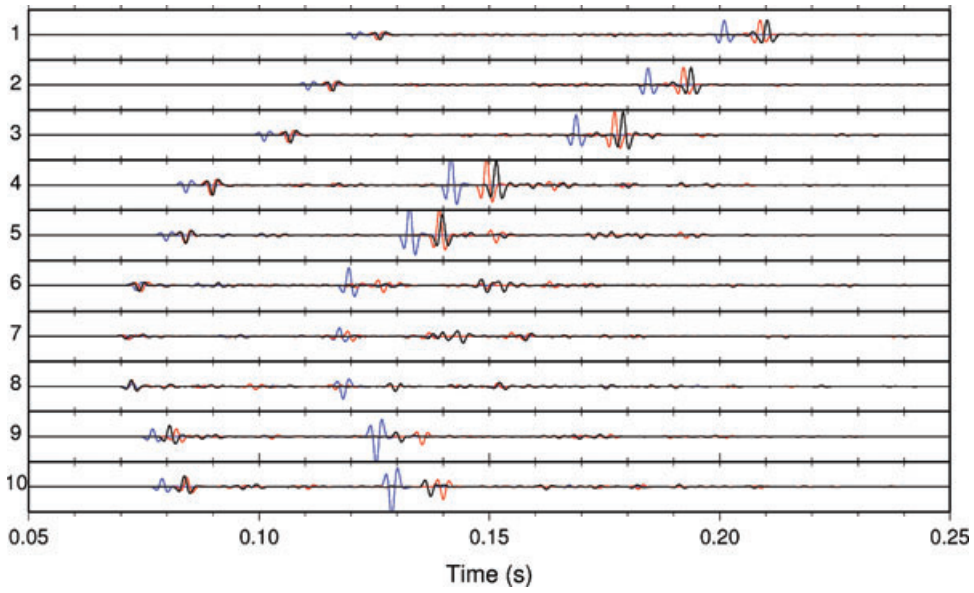

Figure 5 Comparison of 300 Hz waveforms for the surface seismic (blue), VSP (black) and sonic (red) velocity models.

case and in Fig. 5 for the 300 Hz case. There are several observations that can be made when comparing Figs 3-5. First, the P-wave phase arrivals for all velocity models at 40 Hz are approximately equal for geophones 6–8. This is because the raypaths are horizontal and at this low frequency the velocity models for this depth interval are roughly equivalent (i.e., the vertical heterogeneity of the VSP and sonic velocity model are averaged over the approximate 100 m dominant seismic wavelength). As the source frequency increases, the P-wave phase arrivals for geophones 6–8 begin to deviate as the influence of material averaging decreases (i.e., dominant wavelength decreases). Second, for all cases the S–wave phase arrivals differ and this is particularly significant for the surface seismic velocity model. This suggests that the V_p/V_s ratios for each layer in the surface seismic model do not represent consistent V_p/V_s ratios with respect to the VSP and sonic velocity models. Third, as the frequency of the source increases so does the coda and this is expected as the shorter wavelength

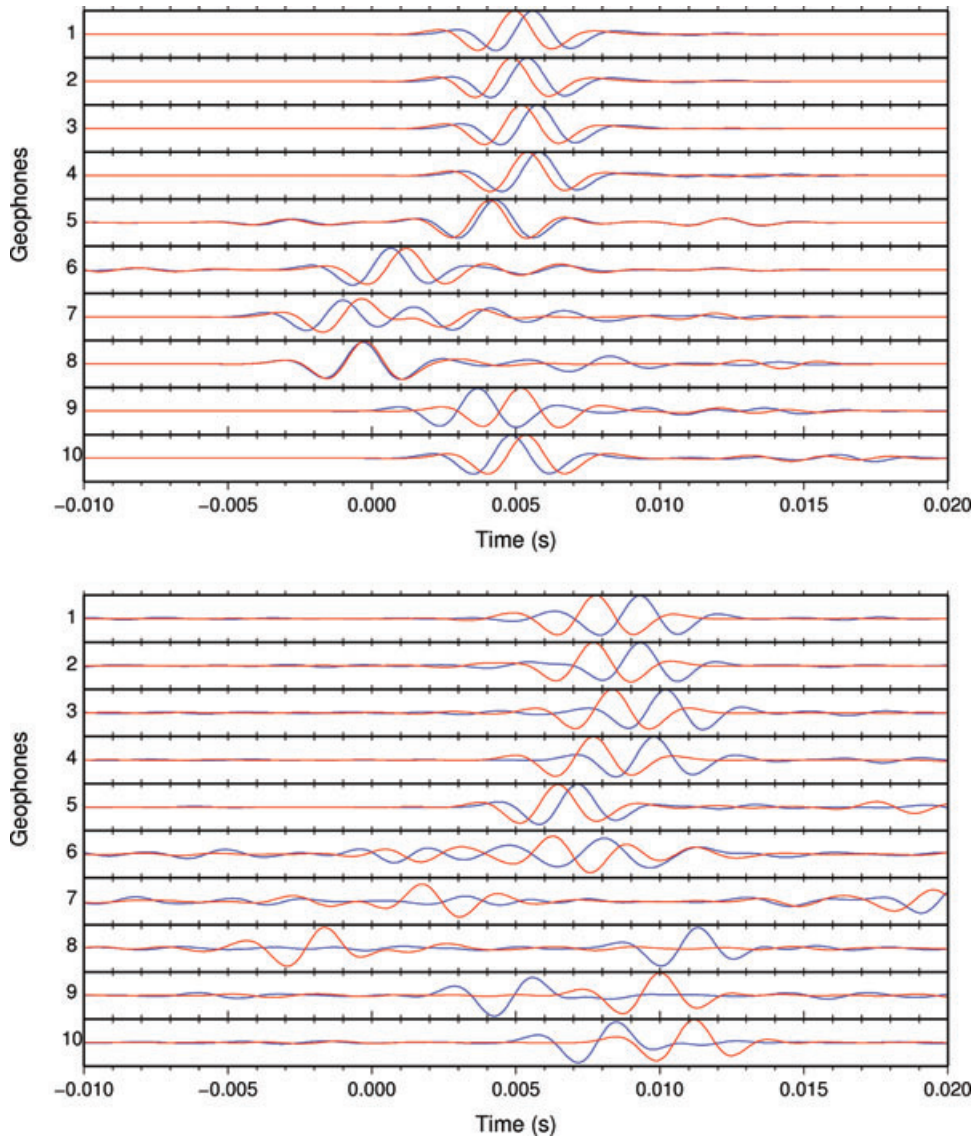

Figure 6 Cross-correlation for the sonic velocity model (blue) and the VSP velocity model (black) at 300 Hz against the surface seismic velocity model: (top) P-wave phase and (bottom) S-wave phase. All the traces show a clear maximum peak, which is the delay with respect to the surface seismic velocity model.

signals are scattered to a much greater degree. Finally, there are noticeable differences between the P- and S-wave phase separation times. This observation may significantly impact location algorithms that are based on the differential P- and S-wave traveltimes.

To measure the phase shifts between all three velocity models in each trace, waveform cross-correlation is performed for the 300 Hz source event. For both the P- and S-wave phases, a 33.6 ms window is applied around the P-wave and S-wave phases. We use the surface seismic velocity model synthetics as the reference time series and perform cross-correlation on the VSP and sonic velocity model synthetics for each geophone. Figure 6 displays the cross-correlation for the P- and S-wave phases between the surface seismic and VSP velocity models and the surface seismic and sonic velocity models. The maximum cross-correlation gives the traveltime difference for the particular phase (P-wave or S-wave) between the velocity models. Table 1 summarizes the results for the 300 Hz source event. The mean P-wave phase shift is 3.5 ms for the VSP velocity model and 3.6 ms for the sonic velocity model.

Table 1 P- and S-wave arrival time differences at 300 Hz between the three-layer model, and the VSP-based model and between the three-layer model and the sonic log-based model. Note that no S-wave picks were possible on geophones 6, 7 and 8 for the VSP-based model data and geophones 6 and 7 for the sonic log-based model data.

	VSP		Sonic	
Geophone	P-wave (s)	S-wave (s)	P-wave (s)	S-wave (s)
1	0.0049	0.0078	0.0056	0.0093
2	0.0049	0.0077	0.0054	0.0093
3	0.0052	0.0083	0.0058	0.0102
4	0.0054	0.0077	0.0058	0.0098
5	0.0041	0.0064	0.0043	0.0071
6	0.0012	NA	0.0007	NA
7	−0.0003	NA	−0.0010	NA
8	−0.0002	NA	−0.0003	0.0113
9	0.0052	0.0100	0.0037	0.0056
10	0.0054	0.0112	0.0048	0.0085

The mean S-wave phase shift is higher, with 8.4 ms for the VSP velocity model and 8.5 ms for the sonic velocity model. For P- and S-wave velocities of 5000 m/s and 3000 m/s, the arrival time differences are equivalent to approximately 20 m in location.

It should be noted that some of the S-wave cross-correlations for geophones 6, 7 and 8 have unrealistically large values (denoted NA in Table 1). In Figs 3–5, it can be seen that the S-wave phases are distinctively different and uncorrelated. This is because the geophones for these traces are located within the minimum amplitude region of the S-wave radiation pattern for the modelled double-couple source mechanism (e.g., Lay and Wallace 1995) and so the waveform amplitudes are very low. Thus the signals being correlated are non-primary arrivals. The results show that both the P- and S-wave phase arrivals vary not only between velocity models but also with microseismic source frequency. The main differences due to the velocity model are changes in the arrival times, whereas the differences due to frequency appear to be the strength of the coda as well as changes in the traveltimes of the P- and S-wave phases. Thus the frequency dependence of coda the could be used to assess the suitability of the velocity model.

Generating synthetics for the second array CGU 21-09 yields similar results. The main difference between these arrays is that well CGU 21-09 is closer laterally and in depth to the synthetic event (see Fig. 2) compared to array CGU 22-09. Figure 7 shows the waveform synthetics for 40 Hz, 150 Hz and 300 Hz source frequencies. Due to the proximity of the array to the synthetic event, the coda at higher frequencies is not as strong compared to the coda developed in the waveforms from well CGU 22-09. However, the phase arrival differences discussed above are still present.

5.2 Sensitivity to source frequency

Having examined the dependence of arrival time on the choice of velocity model, we now examine the effects of source frequency on waveforms and arrival times. In Fig. 8, we plot the simulated waveforms generated using the sonic velocity model and a double-couple source with strike 80° and dip 85° and source frequencies of 40 Hz, 150 Hz and 300 Hz. At 40 Hz frequency, the waveforms are less complex even within the highly heterogeneous sonic velocity model. As the source frequency increases, the waveform complexity increases, with significant increase in the coda. The lower frequencies have larger wavelengths and hence sample a larger velocity space, whereas the higher frequencies have smaller wavelengths and hence are much more sensitive to local velocity variations. Arrival time differences in the phase peaks are also observed in Fig. 8. Focusing on the first break (the first deviation from zero amplitude), the P- and S-wave phases have essentially identical arrival times for all frequencies. However, in practice, ambient and instrument noise in real data would obscure identification of these first breaks.

6 DISCUSSION

Changes in the velocity model cause a systematic change in the arrival time as well as a significant coda trailing the primary P-wave phase. For certain environments, the lithological contrast (even though highly heterogeneous in a petrophysical sense) could be so small that a smooth, weakly heterogenous velocity model is sufficient. Yet in other environments, the elastic contrasts may be large enough that a strongly heterogeneous velocity model is required. With increasing source frequency, the influence of the velocity model increases. This suggests it is important to consider the range of source frequencies of microseismic events as well as the strength of elastic contrasts due to lithology when constructing a velocity model for event location processing. Furthermore, recent work in modelling microseismicity using coupled flow-flow and geomechanical simulation (e.g., Angus *et al.* 2010; Zhao and Young 2012) will require appropriate velocity models to bench mark predictions with microseismic waveform data. Thus an understanding of the influence of the velocity model on microseismic waveforms will guide any necessary

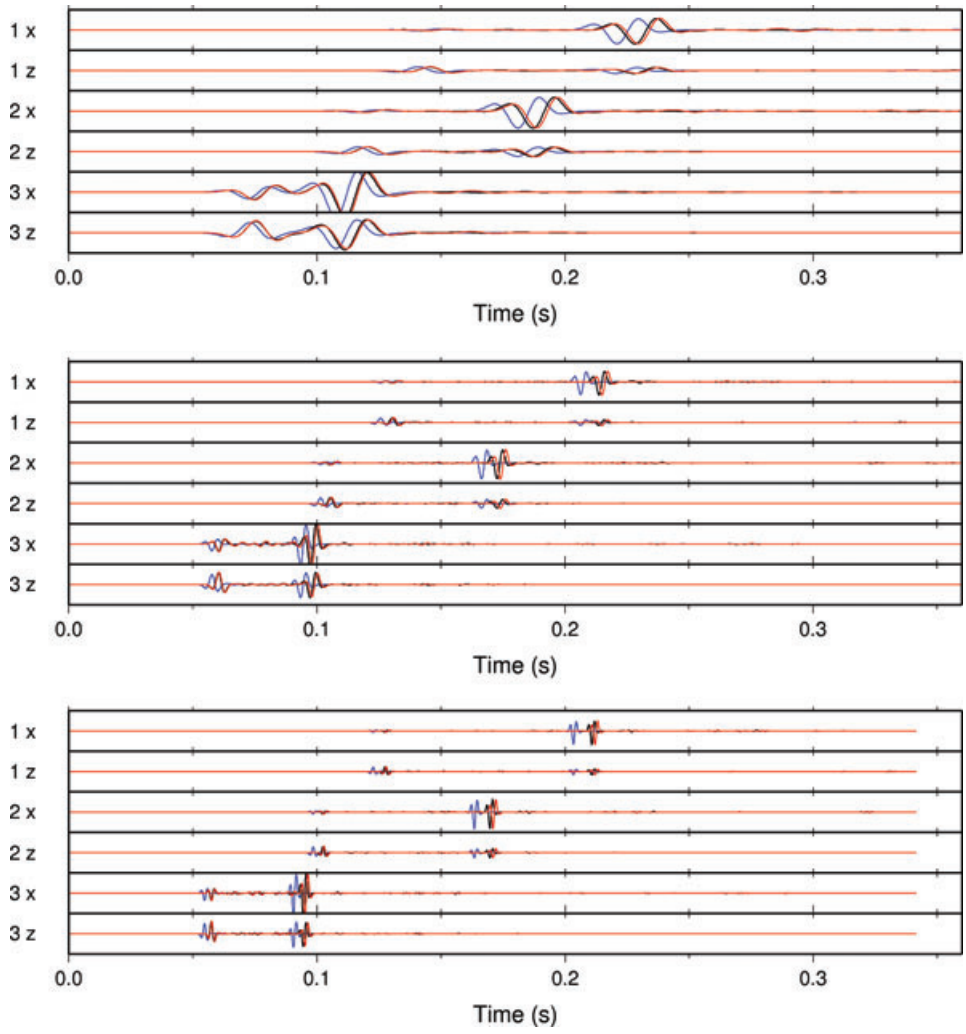

Figure 7 Shows the waveforms for the sonic velocity model for varying frequencies 40 Hz (top), 150 Hz (middle) and 300 Hz (bottom) from the other geophone array. Notice that the coda is less developed compared to the waveforms in well CGU 22-09.

modifications to the synthetic velocity models (e.g., spatial smoothing) used in generating synthetic microseismic waveforms.

The velocities models used show significant variations in velocity in the middle layers so one would expect the arrivals particularly at the central geophones in the array to be different. This is not always the case due to material averaging during wave propagation. In other words, the wavefield has finite-frequency and hence the wavefield is sensitive to a localized volume dependent on the frequency content of the signal rather than limited to an infinitesimal ray.

It is important to note that the variations of arrival times in P- and S-waves (3.5 ms and 8.5 ms respectively) will significantly effect location algorithms, unless errors associated with the velocity model are taken into account. Currently, calibration and perforation shots are typically used to benchmark the location algorithm and velocity model. Any location algorithm that does not take into account errors in the velocity model and finite-frequency effects will significantly underestimate the location error. In essence, this is a fairly obvious observation and relates to the highly non-linear and non-unique characteristic of the location inversion problem.

7 CONCLUSION

We examine the importance of the velocity model and microseismic source frequency on microseismic waveforms using finite-difference waveform synthetics. We simulate waveforms for a source–receiver geometry typical of hydraulic fracture

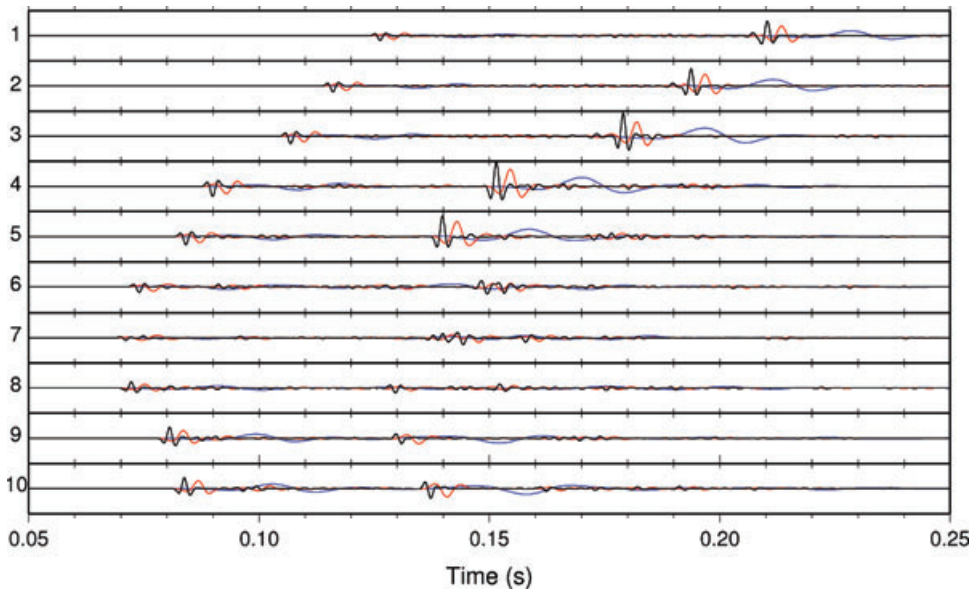

Figure 8 Shows the waveforms for the 40 Hz (blue), 150 Hz (black) and 300 Hz (red) sources and the sonic velocity model. All the wavelets have similar first breaks however the main peak of the wave is delayed more with lower frequency.

programs. Specifically, we model a multilevel borehole array of receivers using a source located horizontally from the array with distance on the order of a few hundred meters. The variations in velocity models manifest in perturbations in arrival times of the P- and S-wave phases of approximately 3.5 ms and 8.5 ms, respectively. The differences in arrival times are equivalent to approximately 20 m in location. As the model heterogeneity and the source frequency increase, the strength of the waveform coda increases.

8 ACKNOWLEDGEMENTS

We would like to thank James Rutledge for providing the well logs and velocity models for the Cotton Valley hydraulic experiment and members of the BUMPS consortium for the helpful discussion of the waveform modelling results.

REFERENCES

Alford R., Kelly K. and Boore D., 1974. Accuracy of finite–difference modeling of the acoustic wave equation. *Geophysics* **39**(6), 834–842.

Al-Rajhi M., Fisher Q.J., Grattoni C. and Angus D.A., 2010. Analysis of Stress Dependent Permeability and Velocity: A Siltstone Core Analogue of a Tight-Gas Reservoir, 2nd Middle East Tight Gas Reservoir Workshop, Bahrain, TG09.

Angus D.A. 1998. *Applicability of moment tensor inversions to mine–induced microseismic data*. Master's thesis, Queen's University, Canada.

Angus D.A., 2005. A one–way wave equation for modelling seismic waveform variations due to elastic heterogeneity. *Geophysical Journal International* **162**, 882–898.

Angus D.A., Kendall J.-M., Fisher Q.J., Segura J.M., Skachkov S., Crook A.J.L. and Dutko M., 2010. Modelling microseismicity of a producing reservoir from coupled fluid-flow and geomechanical simulation. *Geophysical Prospecting* **58**, 901–914.

Baig A. and Urbancic T. I., 2010. Microseismic moment tensors: A path to understanding frac growth. *The Leading Edge* **29**(3), 320–324.

Baig A.M., Urbancic T. I., Guest A., von Lunen E. and Hendrick J. 2011. Evaluating the effectiveness of hydraulic fracture staging with moment tensors: Recovery. 2011 CSPG CSEG CWLS Convention.

Bulant P. and Klimeš L., 2008. Comparison of VSP and sonic-log data in non-vertical wells in a heterogeneous structure. *Geophysics* **73**(4), U19–U25.

Chambers K., Kendall J.-M., Brandsberg-Dahl S. and Rueda J., 2010. Testing the ability of surface arrays to monitor microseismic activity. *Geophysical Prospecting* **58**(5), 817–826.

Clayton R. and Engquist B., 1977. Absorbing boundary conditions for acoustic and elastic wave equations. *Bulletin of the Seismological Society of America* **67**(6), 1529–1540.

Duncan P. and Eisner L. 2010. Reservoir characterization using surface microseismic mon- itoring. *Geophysics* **75**, no. 5.

Dyer B., Jones R., Cowles J., Barkved O. and Folstad P., 1999. Microseismic survey of a North Sea reservoir. *World Oil* **220**(3), 74–78.

Eisner L., Duncan P.M., Heigl W.M. and Keller W.R., 2009. Uncertainties in passive seismic monitoring. *The Leading Edge* **28**(6), 648–655.

Eisner L., Hulsey B.J., Duncan P., Jurick D., Heigl W. and Keller W. 2010. Comparison of surface and borehole locations of induced seismicity. *Geophysical Prospecting* **58**(5), 805–816.

Foulger J. and Julian B., 2012. Earthquakes and errors: Methods for industrial applications. *Geophysics* **76**(6), WC5–WC15.

Gharti H.N., Oye V., Roth M. and Kuhn D. 2010. Automated microearthquake location using envelope stacking and robust global optimization. *Geophysics* **75**(4), MA27–MA46.

Gibowicz S.J. and Kijko A. 1994. *An Introduction to Mining Seismology*. Academic Press.

Izutani Y. and Kanamori H., 2001. Scale–dependence of seismic energy-to-moment ratio for strike–slip earthquakes in Japan. *Geophysical Research Letters* **28**(20), 4007–4010.

Jansky J., Plicka V. and Eisner L., 2010. Feasibility of joint 1D velocity model and event location inversion by the neighbourhood algorithm. *Geophysical Prospecting* **58**(2), 229–234.

Jones G.A., Raymer D., Chambers K. and Kendall J.-M., 2010. Improved microseismic event location by inclusion of a priori dip particle motion: A case study from Ekofisk. *Geophysical Prospecting* **58**(5), 727–737.

Kelly K., Ward R., Treitel S. and Alford R. 1976. Synthetic seismograms: A finite–difference approach.

Larsen S. and Harris D. 1993. Seismic wave propagation through a low-velocity nuclear rubble zone. Lawrence Livermore National Lab.

Lay T. and Wallace T.C. 1995. *Modern Global Seismology*. Academic Press.

Liner C.L. 2004. *Elements of 3D Seismology*. PennWell.

Maxwell S.C., 2009. Microseismic Location Uncertainty. *CSEG Recorder* **34**(4), 41–46.

Maxwell S.C., 2010. Microseismic: Growth born from success. *The Leading Edge* **29**(3), 338–343.

Maxwell S.C., Rutledge J., Jones R. and Fehler M. 2010a. Petroleum reservoir charac-terization using downhole microseismic monitoring. *Geophysics* **75**(5), 75A129–75A137.

Maxwell S.C., Rutledge J., Jones R. and Fehler M., 2010b. Anisotropic velocity modeling for microseismic processing: Part 1 – Impact of velocity model uncertainty. *SEG Technical Program Expanded Abstracts* **29**(1), 2130–2134.

Maxwell S., Shemeta J., Campbell E. and Quirk D. 2008. Seismic deformation rate monitoring. SPE, page SPE134695.

Maxwell S.C. and Urbancic T.I. 2005. The potential role of passive seismic monitoring for real time 4D reservoir characterization. *SPE Reservoir Evaluation and Engineering*, 70–76.

Maxwell S.C., Young R.P., Bossu R., Jupe A. and Dangerfield J. 1998. Microseismic Logging of the Ekofisk Reservoir. SPE/ISRM Rock Mechanics in Petroleum Engineering Conference.

O'Brien J. and Harris R., 2006. Multicomponent VSP imaging of tight-gas sands. *Geophysics* **71**(6), E83–E90.

Pavlis G.L. 1986. Appraising Earthquake Hypocenter Location Errors – A Complete, Practical Approach For Single-Event Locations. *Bulletin of the Seismological Society of Amer-ica* **76**(6), 1699–1717.

Rentsch S., Buske S., Lüth S. and Shapiro S.A., 2007. Fast location of seismicity: A migration-type approach with application to hydraulic-fracturing data. *Geophysics* **72**(1), S33–S40.

Rutledge J.T. and Phillips W.S., 2003. Hydraulic stimulation of natural fractures as revealed by induced microearthquakes, Carthage Cotton Valley Gas Field, East Texas. *Geophysics* **68**(2), 441–452.

Rutledge J.T., Phillips W.S. and Mayerhofer M.J., 2004. Faulting Induced by Forced Fluid Injection and Fluid Flow Forced by Faulting: An Interpretation of Hydraulic-Fracture Microseismicity, Carthage Cotton Valley Gas Field, Texas. *Bulletin of the Seismological Society of America* **94**(5), 1817–1830.

Teanby N., Kendall J.-M., Jones R.H. and Barkved O., 2004. Stress–induced temporal variations in seismic anisotropy observed in microseismic data. *Geophysical Journal Inter national* **156**, 459–466.

Trifu C. I., Angus D. and Shumila V., 2000. A Fast Evaluation of the Seismic Moment Tensor for Induced Seismicity. *Bulletin of the Seismological Society of America* **90**(6), 1521–1527.

Urbancic T.I., Morrish T. and Shumila V. 2009. Understanding hydraulic fracture growth by mapping source failure mechanisms. EAGE Workshop on Passive Seismic, A16.

Urbancic T.I. and Zinno R.J., 1998. Cotton Valley hydraulic fracture imaging project: Feasibility of determining fracture behavior using microseismic event locations and source parameters. *SEG Technical Program Expanded Abstracts* **17**(1), 964–967.

Verdon J.P. and Kendall J.-M. 2011. Detection of multiple fracture sets using observations of shear-wave splitting in microseismic data. *Geophysical Prospecting*, 1–16.

Verdon J.P., Kendall J.-M., White D.J. and Angus D.A., 2011. Linking microseismic event observations with geomechanical models to minimise the risks of storing CO_2in geological formations. *Earth and Planetary Science Letters* **305**, 143–152.

Walker R.N. 1997. Cotton Valley hydraulic fracture imaging project. *Proceedings of the 1997 Society of Petroleum Engineers Annual Technical Conference*.

Zhao X. and Young R., 2012. Numerical modeling of seismicity induced by fluid injection in naturally fractured reservoirs. *Geophysics* **76**(6), WC169–WC182.

Zimmer U., Maxwell S., Waltman C. and Warpinski N. 2007. Microseismic Quality Control Reports as an Interpretive Tool for Non-specialists. SPE Annual Technical Conference and Exhibition.